Shape memory modeling of a nonlinear and superelastic compliant mechanism

Hargrove, Brianne; Nastevska, Angela; Jovanova, Jovana; Frecker, Mary

DOI
10.1115/SMASIS2021-67651

Publication date
2021

Document Version
Final published version

Published in
Proceedings of ASME 2021 Conference on Smart Materials, Adaptive Structures and Intelligent Systems, SMASIS 2021

Proceedings of the ASME 2021 Conference on Smart Materials, Adaptive Structures and Intelligent Systems
SMASIS2021
September 14-15, 2021, Virtual, Online

SMASIS2021-67651

SHAPE MEMORY MODELING OF A NONLINEAR AND SUPERELASTIC COMPLIANT MECHANISM

Brianne Hargrove
The Pennsylvania State University
University Park, PA
bbh5128@psu.edu

Angela Nastevska
Kentaur-Impex
Skopje, North Macedonia
angela.nastevska@kentaur.com.mk

Jovana Jovanova
Delft University of Technology
Delft, Netherlands
J.Jovanova@tudelft.nl

Mary Frecker
The Pennsylvania State University
University Park, PA
mxf36@psu.edu

ABSTRACT

With the shift from traditionally manufactured rigid-body mechanisms to lightweight compliant mechanisms (CMs) in additive manufacturing, researchers have become interested in modeling the behavior of CMs with high flexibility. Due to the large deformations that can be achieved, the use of CMs has expanded into applications such as energy absorption, and in the case of cellular contact-aided compliant mechanisms (C3Ms), stress-relief through self-contact. Although CMs provide greater design freedom in terms of geometry, size, and functionality than their rigid-link mechanism counterparts, there are notable challenges in modeling their complexity. This complexity arises not only from the nonuniform geometry of CMs, but also from variable material properties such as effective modulus. Current research in this area has been primarily limited to the study of linear elastic materials. Thus, there is a need to develop a model that describes CMs with nonlinear material behavior.

The focus of this work is on a low-fidelity model using nonlinear, superelastic materials. In order to account for both geometric nonlinearity and superelasticity, the use of a new pseudo-rigid body model is proposed. The model incorporates the mechanics of shape memory alloy (SMA) behavior in a folding C3M design. The combined application of pseudo-rigid body modeling and SMAs allows for the prediction of large recoverable deformations through superelasticity. In previous work, a segmented pseudo-rigid body model was used to account for the nonlinear behavior of a folding C3M. A mathematical model of the superelastic SMA material is derived based on 2D beam flexure equations. The development of these equations allows for an analysis of the deflection under an applied force. As a part of this study, the results of the SMA model will be compared to high-fidelity finite element simulations as a judge of the accuracy of the analytical model.

Keywords: Cellular contact-aided compliant mechanism, Shape memory alloys, superelasticity

NOMENCLATURE

σ	stress, MPa
ε	strain, m/m
E_A	austenite modulus, GPa
S	modulus during phase transformation, GPa
E_M	martensite modulus, GPa
σ^{Ms}	martensite start stress, MPa
σ^{Mf}	martensite finish stress, MPa
ε_l	maximum residual strain, m/m
x,y,z	coordinates, m
x_1, x_2	phase transition points in x-direction, m
$y_{tr,1}$, $y_{tr,2}$	phase transition points in y-direction, m
a	depth of beam into page in z-direction, m
b	half-thickness of beam, m
L	length of undeformed beam, m
l	projected length of deformed beam, m
s	arc length of deformed beam, m
F	applied force at tip, N
M	internal moment in beam, N·m
κ	curvature along beam, m^{-1}
θ	angle of deflection of beam, degrees
δ_x, δ_y	deflection at the tip of beam in x and y, m
i, j	indices for beam and arc discretization
α, β	interior angles of arc model, degrees
γ	angle of rotation for segmented arc, degrees
ζ	angle of rotation for deformed arc, degrees

$T(x_j,y_j)$	tip positions of segmented arc model, m
R	radius of arc model, m
L_s	length of each segment in arc model, m
MSE	mean-squared error
n	number of segments
N	sample size of tip forces for arc model

1. INTRODUCTION

Recent technological advancements in additive manufacturing, smart materials, and cellular structures have paved the way for innovative designs of structures in terms of shape and functionality. Trends to shift from traditionally manufactured rigid-body mechanisms to the use of additive manufacturing for fabricating lightweight compliant mechanisms (CMs) have raised interest in modeling the nonlinear behavior of CMs. CMs are defined as flexible structures that transmit energy, force and motion through elastic deformation. Many applications can benefit from the availability of large deformations in CMs including energy absorption, path generation and shape change.

A special class of mechanisms are contact-aided compliant mechanisms that rely on incorporated contact surface(s) for non-smooth path generation or tailoring nonlinear structural stiffness [1–3]. Previous research includes metamaterial-like arrays of contact-aided compliant mechanisms called cellular contact-aided compliant mechanisms (C3Ms). The benefits of C3Ms show potential in applications for stress relief [4–6] and energy absorption [7-9]. As C3Ms rely on high compliance for their functionality, combining their geometry with superelastic material behavior (such as Nitinol) can enhance their performance. This combined effort of the geometry and tailored superelasticity by functional grading for energy absorption is demonstrated in [8, 9].

To be able to engineer structures based on C3Ms with nonlinear material properties such as superelasticity, designers rely on complex modeling techniques. The complexity of modeling arises from nonuniform geometry and variable material properties such as effective modulus. A "folding C3M" design from Nitinol based on a semicircular arc and contact surface was investigated for large scale applications [10]. The design was based solely on FEA to account for both material nonlinearity due to superelasticity and geometric nonlinearity due to large deformations. Systematic optimization of a C3M based only on FEA is not feasible as it will require many iterations of computationally intense FEA simulations.

Therefore the focus of this work is on developing a low-fidelity model of CMs with superelastic material behavior and large deformations. The model incorporates the mechanics of shape memory alloy (SMA) behavior in a beam and a folding C3M design. Based on large deflection beam theory and a SMA material model, the deflection under external loading is predicted. As a part of this study, the results of the SMA beam model are compared to high-fidelity finite element simulations as a judge of the accuracy of the analytical model for model validation.

2. MATERIALS AND METHODS

A CM is modeled as a cantilever beam subject to an applied force at its tip, from which the resulting deflection is predicted. The cantilever beam model then serves as the basis for approximating the deflection of a compliant semicircular arc, to which a segmentation approach is applied. Finite element analysis (FEA) is performed to create a comparison between the mathematical and simulated models. First, the SMA material model is introduced in the context of the cantilever beam.

2.1 Shape Memory Alloy (SMA) Material Model

The primary goal of this work is to utilize the superelastic behavior of SMAs and their ability undergo large, yet recoverable, deformations. To study the applicability of SMAs in modeling the large deflection of CMs, Nitinol or NiTi is used as the material model. Figure 1 shows a multilinear material model for Nitinol originally developed by Auricchio et al [11]. E_A, S, and E_M, are the austenite, phase-transition, and martensite moduli respectively. The moduli represent the slopes of the stress-strain curve in each region. The martensite start stress (σ^{Ms}) and finish stress (σ^{Mf}) are the stresses between which phase transformation from austenite to martensite takes place. The maximum residual strain after loading is given by ε_l .

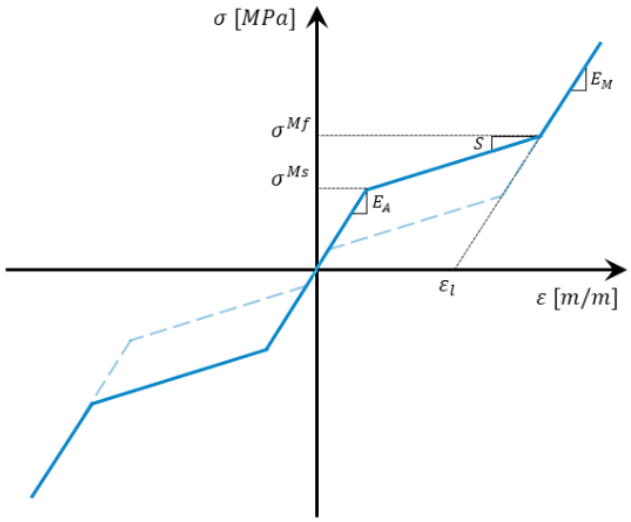

FIGURE 1: STRESS-STRAIN CURVE FOR NITI MATERIAL

Using this multilinear material model, Eshghinejad et al. derived an analytical model for the deflection of an SMA cantilever beam for small deformation [12]. Here, this beam model is adapted and extended to consider large deformations under force, F. As shown in Figure 2, the beam is divided into three regions: (1) $x_2 \leq x \leq L$, which represents the portion of the beam that has not yet experienced the stress-induced phase transformation associated with superelasticty, (2) $x_1 \leq x \leq x_2$, which represents the portion of the beam undergoing phase transformation, and (3) $0 \leq x \leq x_1$, which represents the portion of the beam where phase transformation is complete. The lines, x_1

and x_2, represent the transition points into and out of the stress-induced phase transformation region. The points, $y_{tr,1}$ and $y_{tr,2}$, are the locations where the stress profile changes due to the multilinearity of the SMA material.

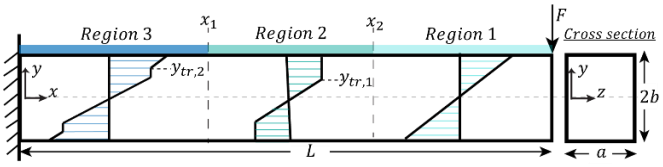

FIGURE 2: STRESS DISTRIBUTION ALONG CANTILEVER BEAM MODEL

In the current paper, unloading is not modeled; only the stress-strain relations for loading are considered. The stress-strain equations for loading are based on a piecewise linear function that is defined for each region of the beam, as proposed in [12] and shown in Eq. 1 as the loading stress (σ):

$$\sigma_i = \begin{cases} Region\ 1:\ E_A\varepsilon & \text{if } \varepsilon < \dfrac{\sigma^{Ms}}{E_A} \\ Region\ 2:\ S\left(\varepsilon - \dfrac{\sigma^{Ms}}{E_A}\right) + \sigma^{Ms} & \text{if } \dfrac{\sigma^{Ms}}{E_A} < \varepsilon < \dfrac{\sigma^{Mf}}{E_M} + \varepsilon_l \\ Region\ 3: E_M(\varepsilon - \varepsilon_l) & \text{if } \varepsilon > \dfrac{\sigma^{Mf}}{E_M} + \varepsilon_l \end{cases} \tag{1}$$

where,

$$S = \frac{\sigma^{Mf} - \sigma^{Ms}}{\dfrac{\sigma^{Mf}}{E_M} + \varepsilon_l - \dfrac{\sigma^{Ms}}{E_A}}$$

In the first region, where the stress distribution is linear, the strain, ε, is below the martensite start strain (σ^{Ms}/ E_A) and the slope of the curve is the austenite modulus. The second region is bounded by the martensite start and finish strain ($\sigma^{Mf}/ E_M + \varepsilon_l$). Beyond the third region, the slope of stress-strain curve is the new, martensite modulus. The mathematical model implemented to derive the behavior of an SMA cantilever beam is described next, using this material model.

2.2 Cantilever Beam Model

Since the model derived by Eshghinejad et al. was applied only for small deformations, it was necessary to extend it to account for large deformations encountered in many CM applications. When a beam is subject to a higher tip load, the deflection is no longer a simple 1D problem, but instead the beam deflects both in the transverse and longitudinal directions due to geometric nonlinearity. Ghuku et al. presented an approach for modeling the large deflection of initially curved beams [13], and an integral approach was derived by Chen for large-deflection beams, which will be applied to this work [14].

As shown in Figure 3, and described in [13], the arc length, s, along the deformed beam varies from 0 to L. However, the new range of x for the deformed beam is from 0 to l, where l is the projected length. The projected length is initially unknown and must be solved iteratively until the condition s(l) = L is met. By this assumption, the original length of the beam does not change under deformation. First, the method used by Eshghinejad et al. to calculate the moment and curvature will be discussed. Following this discussion, the modeling approach for the large deflection of a cantilever beam will be presented.

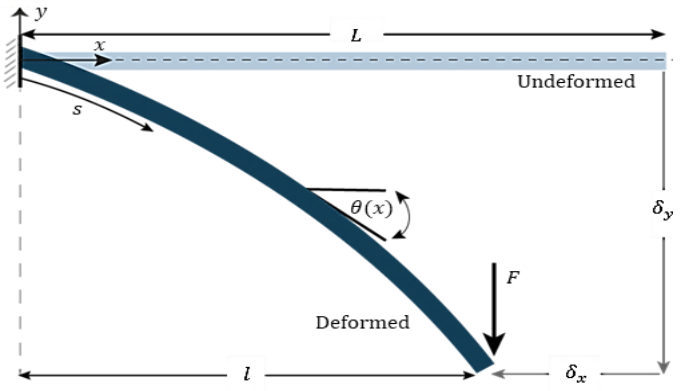

FIGURE 3: CANTILEVER BEAM MODEL FOR LARGE DEFORMATION DUE TO AN APPLIED FORCE

MATLAB is used to implement the analytical model of the cantilever beam. To find the moment as a function of x, the stress is integrated symbolically across the half-thickness of the beam, b, and is multiplied by the depth into the page, a. It is assumed that the stress distribution is symmetric about the neutral axis so that the integrals are multiplied by a factor of two. Eq. 2 defines the moment in a general region of the beam as:

$$M_i(\mathrm{x}) = 2\int_0^b y\sigma_i dA \tag{2}$$

The *i-th* stress and moment is replaced by 1, 2, or 3 depending on the x-position of interest in the beam. As a result, the moment equations are only valid in the region in which they are integrated. M_1 is valid within the range $x_2 \leq x \leq l$, M_2 within the range $x_1 \leq x \leq x_2$, and M_3 within the range $0 \leq x \leq x_1$. The vertical distance, y, is integrated from 0 to the half-thickness of the beam, b. After the stress is applied to the moment equation for each region of the beam, the strain, ε, can be replaced by Bernoulli-Euler beam theory that defines the curvature, $\kappa(x)$, as the slope of the linear strain distribution of Eq. 3:

$$\varepsilon(x, y) = y \cdot \kappa(x) \tag{3}$$

The moment and curvature can be related directly and defined in each section of the beam using Eq. 2 and Eq. 3. In the first region of the beam where the stress distribution is linear, the integration of the stress gives a simple result for the moment. Eq. 4 gives the expression for the moment in this region as:

$$M_1(\mathrm{x}) = 2\mathrm{a}\int_0^b y^2 E_A \kappa(x) dy = \frac{2}{3} E_A a b^3 \kappa(x) \tag{4}$$

The curvature can be solved from Eq. 4 by setting the moment equal to the boundary condition, $F \cdot (l - x)$, since the origin is placed at the fixed end of the beam. The projected length, *l*, is used rather than the length of the undeformed beam, *L*, to account for large deflections. The curvature in the first region of the beam is given by Eq. 5:

$$\kappa_1(x) = \frac{3F(l-x)}{2E_A a b^3} \tag{5}$$

The transition point at phase transformation, x_2, is found by setting Eq. 5 equal to the maximum curvature in the linear region to enforce continuity. From the stress-strain relations defined in Eq. 1, the maximum curvature in this region occurs when $y = b$ and when the strain equals to the strain at transformation, σ^{Ms}/E_A. The maximum curvature is thus given by Eq. 6:

$$\kappa_1(x_2) = \frac{\sigma^{Ms}}{bE_A} \tag{6}$$

Then, the transition point is found in Eq. 7 as:

$$x_2 = -\frac{2E_A a b^3 \left(\frac{\sigma^{Ms}}{E_A b} - \frac{3Fl}{2E_A a b^3}\right)}{3F} \tag{7}$$

In the second region of the beam, where phase transformation occurs, the equations for the moment and curvature are more complex and are solved using symbolic integration. The moment in this region is separated into two integrals, representing the change in the stress distribution at the vertical transition point, $y_{tr,1}$. The integration of the stress is defined in Eq. 8:

$$M_2(\mathrm{x}) = 2\mathrm{a}\int_0^{y_{tr,1}} y^2 E_A \kappa(x) dy + 2\mathrm{a}\int_{y_{tr,1}}^b Sy^2\kappa(x) - Sy\frac{\sigma^{Ms}}{E_A} + y\sigma^{Ms} dy \tag{8}$$

The point, $y_{tr,1}$, is determined by setting the Bernoulli-Euler relation for the strain in Eq. 3 equal to the transformation strain, σ^{Ms}/E_A. Eq. 9 gives the expression for $y_{tr,1}$:

$$y_{tr,1} = \frac{\sigma^{Ms}}{E_A \kappa(x)} \tag{9}$$

The moment is then defined by Eq. 10:

$$M_2 = \mathrm{ab}^2\sigma^{Ms} - \frac{a{\sigma^{Ms}}^3}{3E_A^2\kappa(x)^2} + \frac{2Sab^3\kappa(x)}{3} + \frac{Sa{\sigma^{Ms}}^3}{3E_A^3\kappa(x)^2} - \frac{Sab^2\sigma^{Ms}}{E_A} \tag{10}$$

As was similarly done for the first region of the beam, the moment in the region of phase transformation is equated to the boundary condition, $F \cdot (l - x)$, to derive an equation solely as a function of the curvature, $\kappa(x)$, in Eq. 11.

$$F \cdot (l-x) = \mathrm{ab}^2\sigma^{Ms} - \frac{a{\sigma^{Ms}}^3}{3E_A^2\kappa(x)^2} + \frac{2Sab^3\kappa(x)}{3} + \frac{Sa{\sigma^{Ms}}^3}{3E_A^3\kappa(x)^2} - \frac{Sab^2\sigma^{Ms}}{E_A} \tag{11}$$

The expression of Eq. 11 is multiplied by a factor of $\kappa(x)^2$, and then the coefficients are combined and re-arranged to obtain a cubic equation as a function of the curvature (Eq 12). The coefficients (*A, B, and C)* are substituted in order to find the solution of the cubic equation symbolically. Eq. 12 is used for both the second and third regions of the beam, but the appropriate coefficients are applied in each case:

$$A\kappa(x)^3 + B\kappa(x)^2 + C = 0 \tag{12}$$

where,

$$A = \frac{2Sab^3}{3},$$

$$B = F(x-l) + ab^2\sigma^{Ms} - \frac{Sab^2\sigma^{Ms}}{E_A},$$

$$C = \frac{Sa{\sigma^{Ms}}^3}{3E_A^3} - \frac{a{\sigma^{Ms}}^3}{3E_A^2}$$

Solving the cubic equation, the expression for the curvature is given by Eq. 13:

$$\kappa(x) = \left(\sqrt{\left(\frac{C}{2A} + \frac{B^3}{27A^3}\right)^2 - \frac{B^6}{729A^6}} - \frac{C}{2A} - \frac{B^3}{27A^3}\right)^{1/3} - \frac{B}{3A} + \frac{B^2}{9A^2\left(\sqrt{\left(\frac{C}{2A} + \frac{B^3}{27A^3}\right)^2 - \frac{B^6}{729A^6}} - \frac{C}{2A} - \frac{B^3}{27A^3}\right)^{1/3}} \tag{13}$$

Re-substituting the coefficients of Eq. 12 into Eq. 13 gives the equation of the curvature in the second region of the beam.

In the third region of the beam, after phase transformation is complete, the moment is separated into three integrals, representing the change in the stress distribution at the vertical transition points, $y_{tr,1}$ and $y_{tr,2}$. The integration of the stress is defined in Eq. 14:

$$\begin{aligned} M_3(\mathrm{x}) = 2\mathrm{a}\int_0^{y_{tr,1}} y^2 E_A \kappa(x) dy \\ + 2\mathrm{a}\int_{y_{tr,1}}^{y_{tr,2}} Sy^2\kappa(x) - Sy\frac{\sigma^{Ms}}{E_A} + y\sigma^{Ms} dy \\ + 2\mathrm{a}\int_{y_{tr,2}}^{b} y^2 E_M \kappa(x) - yE_M\varepsilon_l \, dy \end{aligned} \tag{14}$$

The transition point, $y_{tr,2}$, is determined by setting the Bernoulli-Euler relation for the strain equal to the strain after transformation, $(\sigma^{Mf}/E_M + \varepsilon_l)$, and solving for $y_{tr,2}$ (Eq. 15):

$$y_{tr,2} = \frac{(\sigma^{Mf}/E_M + \varepsilon_l)}{\kappa(x)} \tag{15}$$

The moment in the third region is solved for symbolically similar to Eq. 10, and the curvature can be determined using the same approach of setting the moment equal to the boundary condition of the applied tip force as done in Eq. 11. The newly found coefficients *(A, B, and C)* from Eq. 12 are substituted into Eq. 13. The expressions for the moment and curvature become functions of only the unknown projected length, *l*, and *x*.

To determine the deflection of the beam, the expression of the curvature for large deflection is used, as given by Eq. 16:

$$\kappa(x) = \frac{d^2y/dx^2}{[1 + (dy/dx)^2]^{\frac{3}{2}}} \tag{16}$$

Chen [14] provides a method to simplify this curvature expression by substituting $z = dy/dx$ to obtain Eq. 17:

$$\kappa(x) = \frac{dz/dx}{\left[1 + z^2\right]^{3/2}} \tag{17}$$

From trigonometric relationships, the curvature can also be expressed as a function of θ, which is the angle of deflection. Eq. 17 and Eq. 18 are used to relate the curvature to the deflection angle, continuing under the assumption of large deflection:

$$\sin\theta = \frac{dy}{ds} \tag{18}$$

where,

$$ds = \sqrt{dx^2 + dy^2}$$

The differential arc length, *ds*, is related to the differential lengths, *dx* and *dy*, by Pythagorean theorem. Simplifying this expression and using that $z = dy/dx$, Eq. 18 becomes Eq. 19:

$$\sin\theta = \frac{dy/dx}{\sqrt{1 + (dy/dx)^2}} = \frac{z}{\sqrt{1 + z^2}} \tag{19}$$

The expression for $\sin\theta$ is the integral of the curvature given in Eq. 14. The deflection angle is then described by Eq. 20:

$$\theta(x) = \arcsin\left(\int \kappa(x) dx\right) \tag{20}$$

The trapezoidal integration method is used to approximate all integrals. To find the deflection angle for a given point along the beam, numerical integration is performed across small divisions of width, *dx*. These values are summed together in a separate variable, from which the integrated points are subtracted to obtain the actual value of $\theta(x)$. This approach was adapted from the work of Hsu in the derivation of moment-curvature and deflection relationships for a nonlinear material [15].

In order to account for large deflections, the projected length, *l*, has to be solved iteratively under two constraints: (1) the value of the arc length at the tip of the beam is approximately equal to the original length, or $s(l) \approx L$, and (2) the integral of the curvature is less than 1 so that Eq. 20 can be solved. The second condition is inherently critical to meet the first condition. The arc length, is defined by Eq. 21:

$$ds = \sqrt{dx^2 + dy^2} = \sqrt{1 + (dy/dx)^2}\, dx \tag{21}$$

Taking the integral of both sides of Eq. 22, with $z = dy/dx$:

$$\int ds = \int \sqrt{1 + z^2}\, dz \tag{22}$$

Chen relates the arc length, *s*, to the curvature by Eq. 23:

$$s = \int \frac{dx}{\sqrt{1 - \left(\int \kappa(x)\, dx\right)^2}} \tag{23}$$

The projected length is solved for iteratively until the maximum value of $\int \kappa(x) dx$ is less than 1. It is defined as the original length, *L*, subtracted by an initial guess, δ_x (Eq. 24):

$$l = L - \delta_x \tag{24}$$

This guess primarily affects the speed of the iterative solver. For this reason, a binary search algorithm is implemented to search for the value of δ_x between 0 and L. In calculating the moments and curvatures, the transition points are also subtracted by this guess to account for the deformation of the beam, as shown in Eq. 25:

$$x_1^* = x_1 - \delta_x$$
$$x_2^* = x_2 - \delta_x \tag{25}$$

The first condition is met iteratively to make the arc length value at the tip, *s(l)*, as close to L as possible. The stopping criterion for this condition is when the error between *s(l)* and L is less than a suitable tolerance. After the solver converges such that $s(l) \approx L$, the final values for the integral of the curvature are used to calculate the y-deflection, y.

The y-deflection is related to the curvature by Eq. 26 [14]:

$$y = \int \frac{\int \kappa(x)\, dx}{\sqrt{1 - \left(\int \kappa(x)\, dx\right)^2}} dx \tag{26}$$

In terms of evaluating the accuracy of the analytical solution, the error at the tip of the beam is calculated for the projected length, *l*, the arc length, *s(l)*, and the y-deflection at the tip, δ_y. The FEA model is used as the exact solution from which these errors are evaluated. For example, the percent error for the y-deflection at the tip is defined as $100\% \cdot \left|(\delta_y - \tilde{\delta}_y)/\tilde{\delta}_y\right|$, where δ_y and $\tilde{\delta}_y$ are the projected lengths of the analytical and FEA models respectively.

Next, the cantilever beam is extended to model more complex CM geometries by segmenting a semicircular arc into small cantilever beam segments.

2.3 Approximation of Arc with Segmentation

The solution for the cantilever beam model is used to approximate the deflection of a semicircular arc by utilizing the approach of segmentation. The goal of the segmentation is to approximate the deformation of the arc by using the model of the cantilever beam previously explained in this paper. For this, the arc is divided into *n*-number of segments, each represented by one cantilever beam as marked in red in Figure 4. Each segment is defined by the angle, α_j, which is calculated as in Eq 27:

$$\alpha_j = \frac{\pi}{n} \tag{27}$$

In this paper, the angle α_j is considered to be the same for all segments ($\alpha_j = \alpha$), so geometrically, the beams comprise a polygon inscribed in a semicircle. The subscript, j, ranges from 1 to n. The side of the polygon or the length of one segment, L_s, is defined by Eq. 28.

$$L_s = 2R\sin\frac{\alpha}{2} \tag{28}$$

The arc defined by the radius, R, and its segments are shown in Figure 4. The global coordinate system is established at the origin by the coordinates x_g and y_g. The local coordinate system is represented by coordinates x_j and y_j. The tip location at the end of each segment in the local coordinate system is $T_j(x_j,y_j)$.

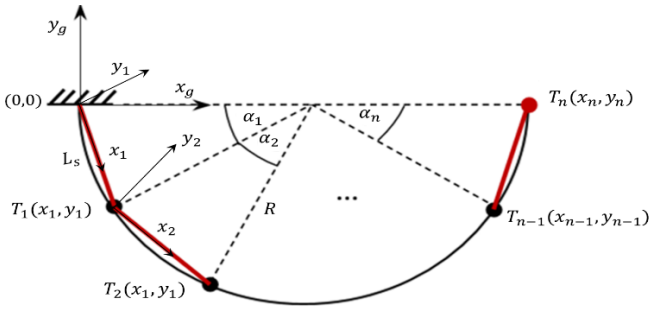

FIGURE 4: SEGMENTATION OF THE ARC IN N-NUMBER OF SEGMENTS, EACH APPROXIMATED WITH A CANTILEVER BEAM

Since each beam is rotated with respect to the global coordinate system (x_g, y_g) in the undeformed state, the position of each beam can be calculated by projecting the length of the segment with the angle ζ_j, which is defined between the segment and the global horizontal axis, as shown in Figure 5(a). After the deformation of the arc, the segments are additionally rotated by the angle θ_j. In this case, the angle defined between the segment and the x-axis is the angle, γ_j, shown in Figure 5(b). This is the angle of rotation between the global and local coordinate systems. The position of the tip of the *j-th* segment after the deformation is calculated using Eq. 29 and Eq. 30:

$$x_j = L_s \cos\gamma_j \tag{29}$$
$$y_j = -L_s \sin\gamma_j \tag{30}$$

The angle γ_j, shown in Figure 5(b), can be calculated as the sum of the angle before the deformation, ζ_j, and the angle that accounts for the deformation, θ_j (Eq. 31). The sign of the angle, θ_j, in Eq. 31 depends on the direction of the load and is positive when the force is directed in the negative y direction.

$$\gamma_j = \zeta_j \pm \theta_j \tag{31}$$

The angle, ζ_j, marked in red in Figure 5(a), depends on α and the angle between the first segment and the global x-axis, β (Eq. 32).

$$\zeta_j = \beta - \alpha(j-1) \tag{32}$$

Since the radius is constant, each triangle shown in Figure 5(a) is isosceles and therefore the angle, β, is calculated in Eq. 33 as:

$$\beta = \frac{\pi - \alpha}{2} \tag{33}$$

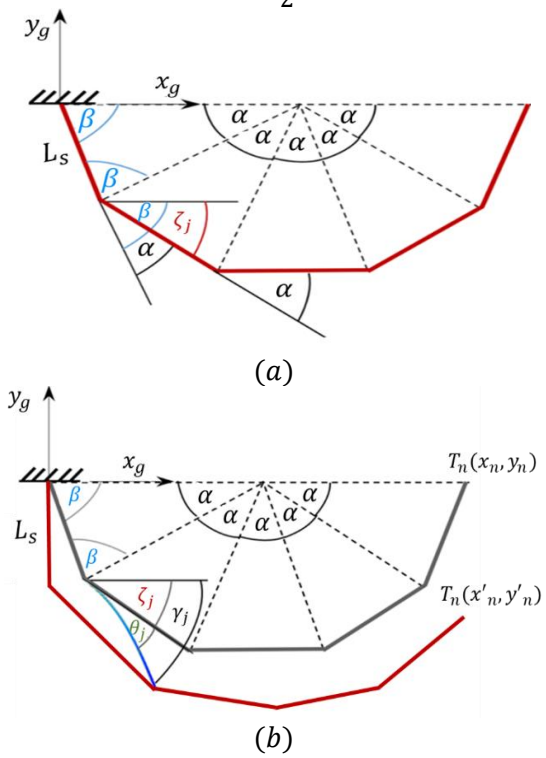

FIGURE 5: ANGLES OF THE SEGMENTED ARC MODEL IN THE UNDEFORMED (A) AND DEFORMED STATE (B)

As aforementioned, when a load is applied, the segments bend and are additionally rotated with respect to the x-axis of the global coordinate system by the angle, θ_j, shown in Figure 5(b). This angle is different for each segment along the arc. In order to calculate this angle, Eq. 20 for the angle of deflection along the cantilever beam was used. Namely, each segment defined in the local coordinate system of the arc is considered to be a segment of a cantilever beam in the global coordinate system, with a total length equal to $L = nL_s$, as shown in Figure 6(a). When it is loaded with the same force that loads the arc, the beam deforms. The slope of the beam changes with the position on the beam along the x-axis, as shown in Figure 6(b). In this way, after the deformation, each segment at its end has a slope that is equal to the slope of the beam at a point $s_j = jL_s$.

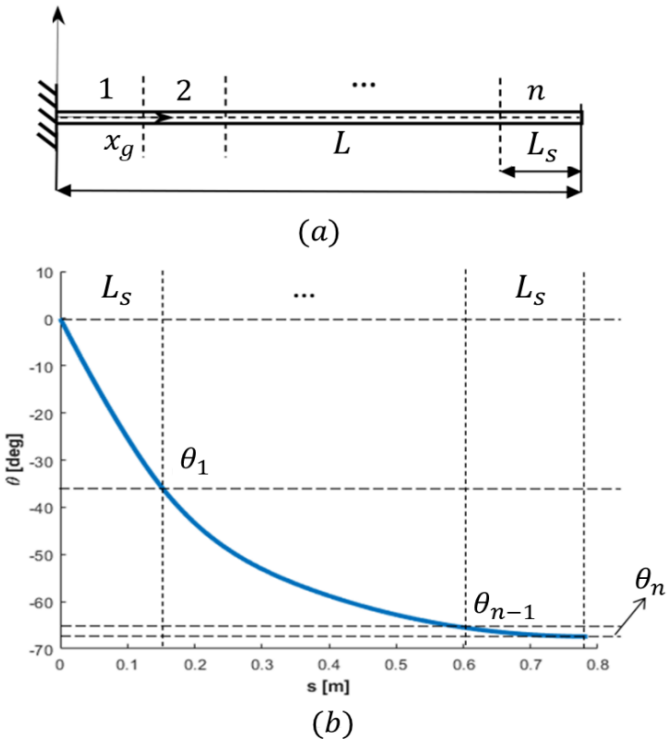

FIGURE 6: SEGMENTS OF A CANTILEVER BEAM LOADED WITH A TIP LOAD (A) AND CALCULATION OF THE SLOPE AT THE END OF EACH SEGMENT (B)

For validation of the segmented arc model, the results for the position of the tip of each segment (i.e., its x and y coordinates), as a function of increasing tip load, are compared to results from FEA discussed in the next section. The mean-squared error, *MSE*, of the deflection profile is calculated between the analytical and FEA arc models using Eq. 34:

$$MSE = \frac{1}{N}\sum_{i=1}^{N}(y - \tilde{y})^2 \tag{34}$$

The variables, y and $\tilde{y}$, represent the y-coordinates of the analytical arc model and FEA model respectively. The sample size, *N*, or the data points of the arc tip position as it is deflected, corresponds to the increasing the tip load applied to the arc model. Next, the details of the FEA study performed for the cantilever beam and arc model are presented.

2.4 Finite Element Analysis

FEA models of the cantilever beam and the semicircular arc were developed in COMSOL Multiphysics using the structural mechanics module. The FEA model is analyzed in 2D with an out of plane thickness of 5 cm. Geometric nonlinearity is included, and the models are solved with a fully coupled approach. The NiTi material model shown in Figure 1 is used with the parameters shown in Table 1 in the following section. The superelasticity is accounted for using this material model.

The length of the base geometry of the cantilever beam is 50 cm and the thickness is 1 cm, loaded with a force ranging from 0 to 10 kN with a step of 5 N. The inner radius of the arc is 22 cm, and the thickness is 3 cm. The load for the arc model is again a force applied at the tip ranging from 0 to 40 kN with a step of 100 N. The mesh for both models is an automatic, physics-controlled mesh with a maximum element size of 0.005 m and minimum element size of 1.0E-5 m.

3. RESULTS AND DISCUSSION

This section outlines the results for the large deflection of the cantilever beam model, followed by the results for the segmented arc model. Both analytical models are compared with FEA to judge the accuracy of the proposed solution methods.

3.1 Cantilever Beam Model and FEA

For the selected SMA, the elastic moduli, martensite start stress σ^{Ms}, and martensite finish stress σ^{Mf} shown in Table 1 are extracted from the multilinear material model of NiTi in Figure 1. The maximum residual strain, ε_l, is extrapolated by extending the line representing the slope, E_M, to the x-axis. These parameters are substituted into the moment, curvature, and transition point equations presented in Eqs. 4-15.

Table 1: PARAMETERS FOR MATERIAL MODEL

E_A	71.4 (GPa)
E_M	69.2 (GPa)
σ^{Ms}	900 (MPa)
σ^{Mf}	1500 (MPa)
ε_l	0.032 (m/m)

The parameters given in Table 2 are used for the baseline cantilever beam model for a tip load of 10 kN. The numerical values of the moment, curvature, and transition points are calculated using the parameters described in Table 1 as well as in the following Table 2.

Table 2: INITIAL PARAMETERS FOR CANTILEVER BEAM

L	50 (cm)
a	5 (cm)
b	0.5 (cm)
F	10 (kN)

The moment and curvature of the cantilever beam are shown in Figures 7(a) and (b). The curvature of the analytical model is compared both with the linear elastic solution of a cantilever beam and the FEA model. For the linear elastic beam, an elastic modulus that is the average of the martensite and austenite moduli is used. From the nonlinear curvature as a function of the projected length, $\kappa(x)$, in Figure 7(b), it can be seen that the analytical model is a suitable predictor of the beam behavior compared to the FEA model. Both models show a slope change marking the phase transformation in region 2 and the completed phase transformation in region 3. The transition points at which the phase transformation begins and ends are marked by the dotted vertical lines on the plot, x_1 *and* x_2, respectively. For the analytical model, x_1 is 0.0365 m and x_2 is 0.1147 m.

In the FEA solution, there was a spike in the curvature at the fixed end which is attributed to a numerical error due to the fixed constraint and the effect of a nonzero Poisson's ratio on the deformation of the beam. Mesh refinement did not appear to change this result, but adding a fillet at the support of the beam or using a Poisson ratio of zero could resolve the singularity. In Figure 7(b), the data corresponding to this spike was instead removed near the fixed end.

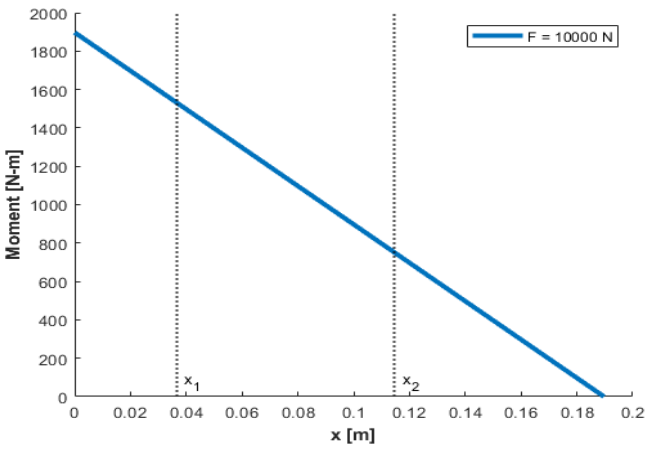

(a)

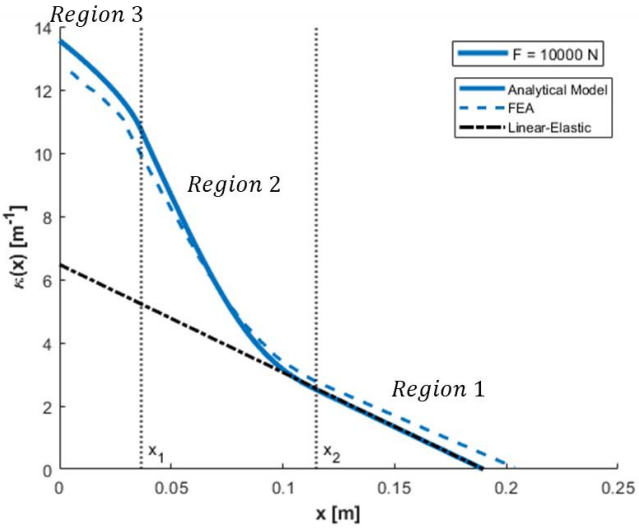

(b)

FIGURE 7: MOMENT ALONG DEFORMED CANTILEVER BEAM (A) AND CURVATURE PROFILES COMPARING THE ANALYTICAL BEAM MODEL WITH A LINEAR-ELASTIC BEAM SOLUTION AND FEA (B) FOR A FORCE OF 10000 N

The analytical model was used to conduct parameter variation studies. First, five different forces were used as the tip load. The plot of the curvature for the analytical and FEA models, in Figures 8(a) and (b), demonstrates how large of a force is needed for phase transformation to begin, i.e., the curvature, $\kappa(x)$, becomes nonlinear. Smaller forces, such as 100

N, 500 N, and 2000 N result in the stress distribution being linear and it is expected that the curvature would also be a linear function of x in these cases.

When the force is increased, the stress becomes significant enough to induce phase transformation, which is shown by the dramatic change in slope of the curvature. The magnitude of the force also has a similar effect on the angle of deflection, in Figure 8(c), behaving as a small-deforming beam when the force is low and exhibiting large deformations with an increase in force.

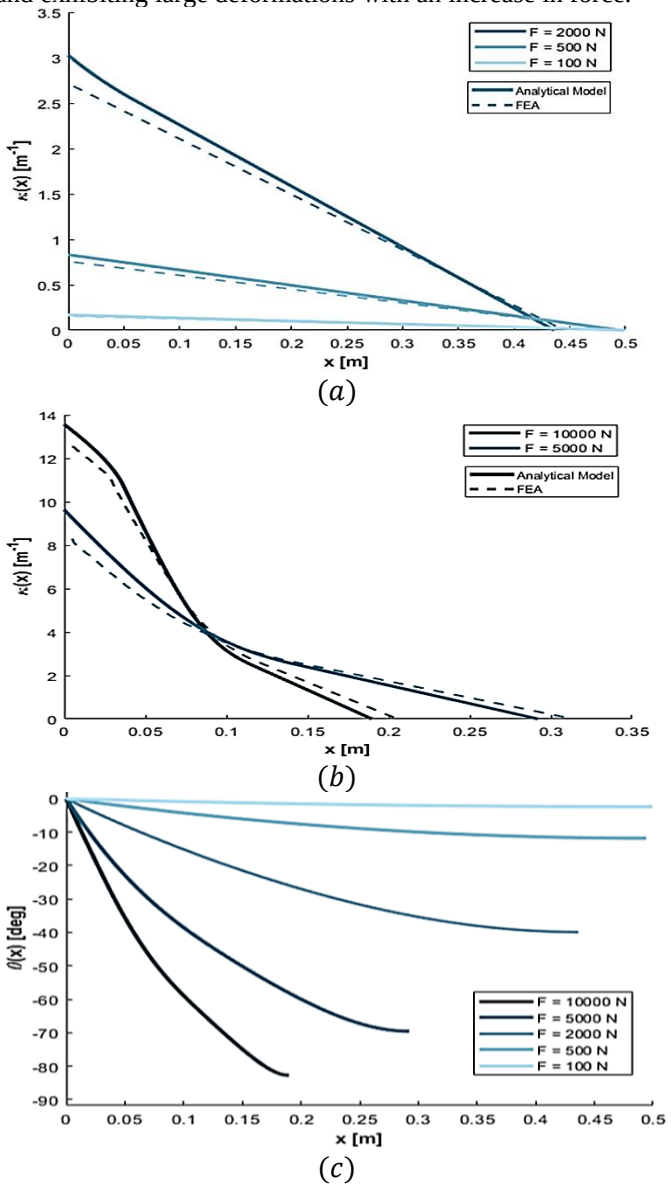

FIGURE 8: CURVATURE ALONG DEFORMED CANTILEVER BEAM (A,B) AND ANGLE OF DEFLECTION (C) FOR INCREASING TIP LOAD

The deflection of the cantilever beam was compared with FEA, as shown in Figure 9(a) and (b). Both studies involved calculating the deflection of the neutral axis of the cantilever beam (1) along the projected length dimension, x, and (2) along the arc length, s. The y-deflection is the same along both x and s.

There was good agreement between the original length, L = 0.5 m, and the value of $s(l)$, as shown in Table 3. There was also an increase in error between the projected lengths of the analytical and FEA models. Figure 9(a) shows that the analytical model underestimates the projected length as the force enters the range where phase transformation occurs. For smaller forces, in the linear range, the error is nearly trivial. The analytical and FEA models are in much better agreement along the arc length in Figure 9(b), where the two curves nearly overlap in most of the load cases.

As shown by Figure 9(a) and Table 3, the x-coordinates of the analytical and FEA models do not align exactly. To accurately find the error between the models, the x-coordinates of the FEA data were linearly interpolated within the analytical data and the y-deflections at these x-coordinates were extracted. Since the analytical model does not reach the same final x-coordinate as the FEA model, due to the solver being an iterative guess of the projected and arc lengths, the y-deflection was extrapolated linearly for these values. Then, the error could be calculated between the two models over the same x-coordinates.

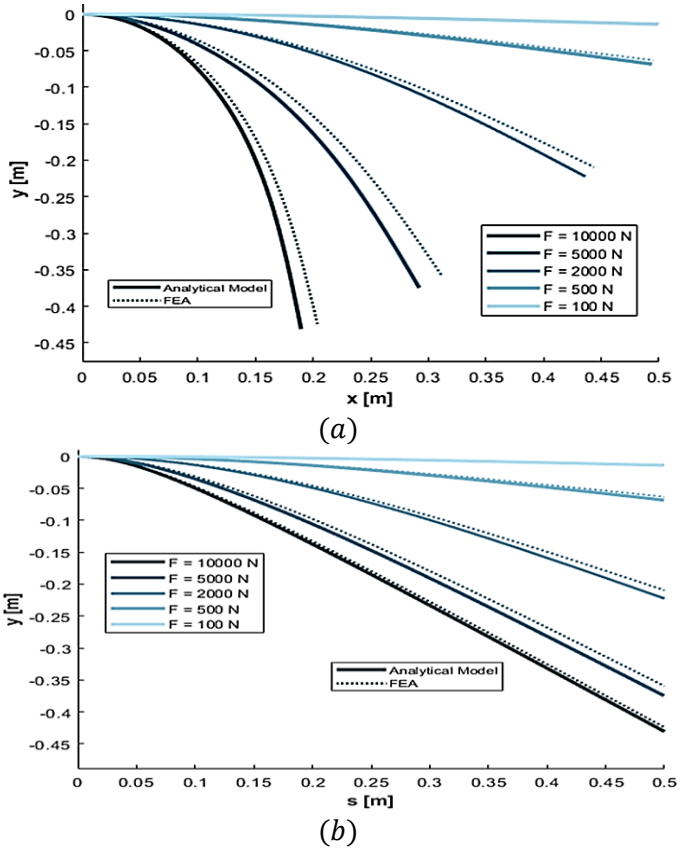

FIGURE 9: Y-DEFLECTION OF CANTILEVER BEAM AS A FUNCTION OF THE PROJECTED LENGTH, l, (A) AND THE ARC LENGTH, s (B)

The y-deflection with respect to s is used in calculating the error between the models. This is done because extrapolating the y-deflection with respect to x introduces additional error to that shown in Table 3. The percent error of the tip y-deflection, δ_y,

and mean-squared error (per Eq. 34) for increasing force is given in Table 4. It is observed that there is better agreement in the y-deflection for larger tip loads, in contrast to the trend shown for the projected length in Table 3. The extent of error depends on which measure of error and which load case are used, but in any case, the error is less than 9%.

Table 3: PROJECTED AND ARC LENGTHS OF THE ANALYTICAL AND FEA MODELS AND PERCENT ERROR FOR INCREASING TIP LOAD

F (N)	l_{anly} *(m)*	l_{FEA} *(m)*	*Error in l* (%)	$s(l)_{anly}$ *(m)*	*Error in* s(*l*) (%)
100	0.4998	0.4998	0.0064	0.5000	9.79e-4
500	0.4944	0.4952	0.1538	0.5001	1.71e-2
2000	0.4362	0.4437	1.7030	0.5000	8.01e-3
5000	0.2922	0.3123	6.4462	0.5000	7.60e-3
10000	0.1897	0.2038	6.9100	0.4993	0.1425

Table 4: PERCENT ERROR OF Y-DEFLECTION AT THE TIP AND MEAN-SQUARED ERROR OF THE DEFLECTION PROFILE FOR INCREASING TIP LOAD

F (N)	*Error in* $\delta_y(s)$ (%)	MSE
100	8.8672	3.078e-7
500	8.6039	6.996e-6
2000	6.1293	4.158e-5
5000	4.3393	8.839e-5
10000	1.5311	1.884e-5

The effect of changing geometric parameters, such as thickness, was studied to determine the scalability of the analytical beam model in how accurately it could evaluate the deflection. In this case, the original half-thickness, *b*, was multiplied by a factor of 1.5 and a factor of 2, as shown in Figure 10. This increase in thickness also increases the bending stiffness of the beam, and consequently decreases the deflection. From the previous study, when the tip load is decreased, the trend suggested that the error in the y-deflection along the beam increased. In other words, the analytical model appears to be more precise for large deformations. Thus, for a change in the half-thickness, it would be relevant to see if a similar trend exists. The applied tip load remains a constant value of 10 kN for this analysis.

In Table 5, there is not a clear trend in the percent errors, but the error is still less than 9% and the MSE is considerably small in each case. As shown in Table 6, the error in the tip deflection decreases when the half-thickness of the beam is small, i.e., when the deflection is large. Thus, a change in the half-thickness of the analytical model depicts a similar trend as a change in the tip load shown in Table 4. For the original half-thickness, b = 0.5 cm, the analytical model is the most accurate based on the percent error of the y-deflection at the tip and the MSE being the lowest out of the three cases. For half-thicknesses larger than 0.75 cm, the model may not be as precise.

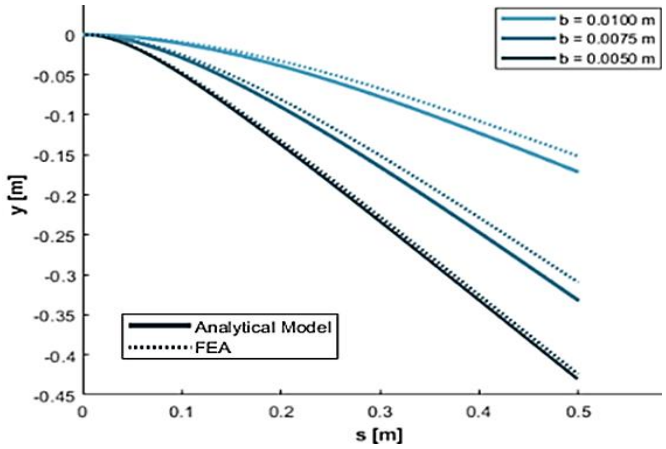

FIGURE 10: COMPARISON OF DEFLECTION FOR ANALYTICAL MODEL WITH FEA FOR INCREASING HALF-THICKNESS, *b*

Table 5: PROJECTED AND ARC LENGTHS OF THE ANALYTICAL AND FEA MODELS AND PERCENT ERROR FOR INCREASING HALF-THICKNESS

b (cm)	l_{anly} *(m)*	l_{FEA} *(m)*	*Error in l* (%)	$s(l)_{anly}$ *(m)*	*Error in* s(*l*) (%)
0.500	0.4998	0.4998	0.0064	0.5000	9.79e-4
0.750	0.3502	0.3720	7.1658	0.5000	6.70e-3
1.000	0.4641	0.4717	1.6153	0.5000	4.40e-3

Table 6: PERCENT ERROR OF Y-DEFLECTION AT THE TIP AND MEAN-SQUARED ERROR OF THE DEFLECTION PROFILE FOR INCREASING HALF-THICKNESS

b (cm)	*Error in* $\delta_y(s)$ (%)	MSE
0.500	1.5311	1.884e-5
0.750	7.1650	1.576e-4
1.000	12.843	1.055e-4

3.2 Segmented Arc Model and FEA

The analytical semicircular arc model is derived from the segmentation of a cantilever beam as shown in Figure 6(a). For the case of the tip of the arc subject to a load of 40 kN, the plot of the curvature along the beam (Figure 11) shows that phase transformation occurs because both transition points, x_1 = 0.0693 m and x_2 = 0.2452 m, can be calculated. This is verified by the von Mises stress distribution of the deformed FEA model, shown in Figure 12, where the highest measured stress is greater than 1600 MPa which is beyond the martensitic finish stress of NiTi (1500 MPa). Again, the curvature profile is compared between the analytical, FEA, and linear elastic solutions.

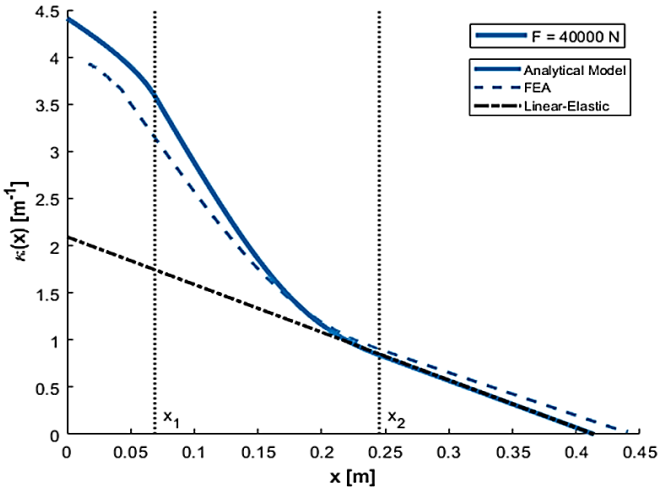

FIGURE 11: CURVATURE PROFILE OF ANALYTICAL, FEA, AND LINEAR-ELASTIC BEAM TO REPRESENT SEGMENTED ARC MODEL BEHAVIOR

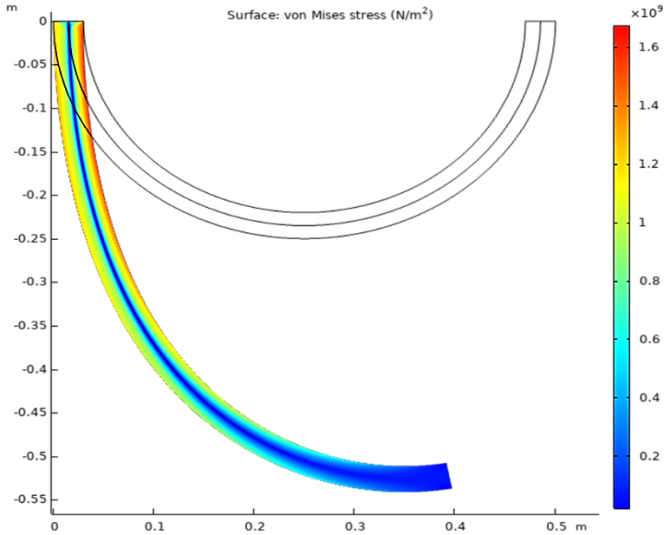

FIGURE 12: VON MISES STRESS DISTRIBUTION OF FEA ARC MODEL FOR A FORCE OF 40000 N

As described previously, the angle of deflection of the cantilever beam model is used in the deformation of the arc model. This angle is discretized along the beam and is used as the deflection angle of each segment, θ_j, as shown in Figure 5(b). As the number of segments is increased, the value of θ for each segment lies over a smaller interval. This would suggest that the approximation of the entire arc model could become more precise as, eventually, the segments are short enough to capture sufficient points on the plot of $\theta(x)$, shown in Figure 6(b).

Figure 13(a) shows the tip deflection of the FEA arc model, from its original shape shown in green to its deformed shape shown in blue. The tip of the arc is taken at the neutral axis of the beam. Then, the tip deflection determined in FEA was compared with the analytical model by gradually incrementing the force from 0 to 40 kN to extract the tip positions. To examine the effect of the number of segments, *n*, on the accuracy of the analytical arc model, the deflection was calculated for increasing number of segments from n = 2 to n = 24. The parameters outlined in Table 7 are used to find the deflection profile of the arc. As expected, a small number of segments is a poor approximation of the arc, and increasing the number of segments improves the agreement of the analytical model with FEA, as shown in Figure 13(b).

Table 7: BASELINE PARAMTERS FOR ARC MODEL

R	25 (cm)
a	5 (cm)
b	1.5 (cm)
F	40 (kN)

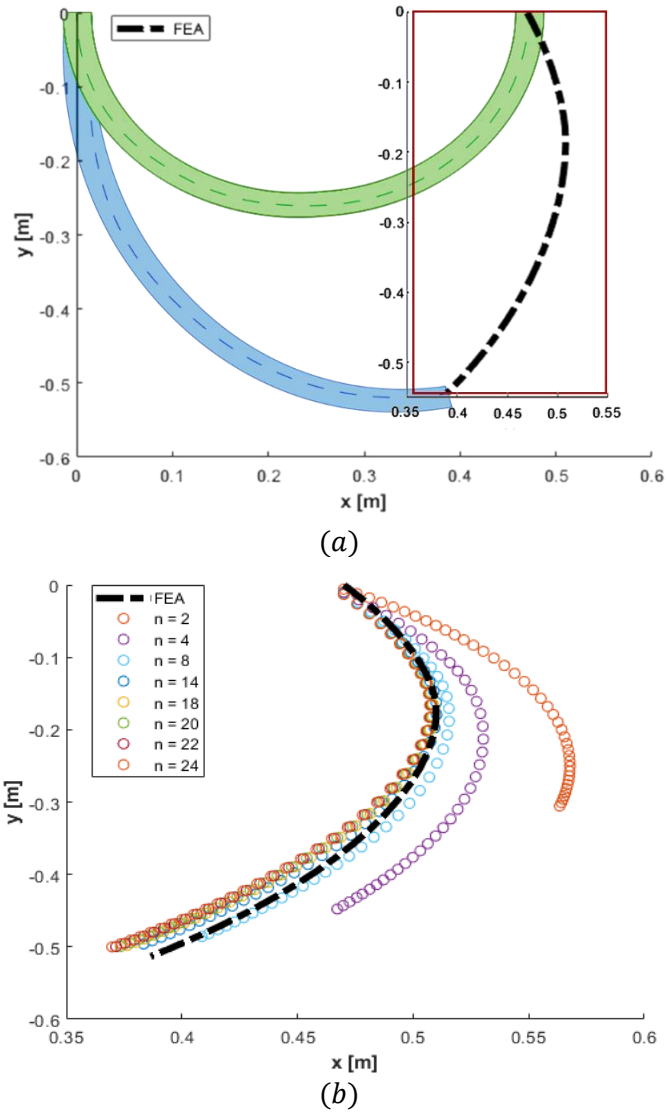

FIGURE 13: DEFLECTION AT THE TIP, $T(x_n, y_n)$, OF THE FEA ARC MODEL FROM AN UNDEFORMED TO DEFORMED STATE (A) AND COMPARISON OF TIP DEFLECTION OF ANALYTICAL ARC MODEL WITH FEA FOR INCREASING NUMBER OF SEGMENTS, *n* (B)

The mean-squared error of the x-deflection of the analytical and FEA models, in Table 8, shows that the error decreases as the number of segments increases from n = 2 to n = 22. Beyond n = 24 segments, the mean-squared error begins to deviate again from the exact solution. This finding could be a result of the analytical model becoming less accurate when the length of the segments is not large enough to represent the deflection. For this reason, the remaining models of the semicircular arc are approximated using n=20 segments since the error is considerably trivial when compared to n = 18 or n = 22 segments.

Table 8: MEAN-SQUARED ERROR BETWEEN ANALYTICAL AND FEA ARC MODEL DEFLECTION PROFILES

Number of segments (n)	*MSE*
2	6.9952E-3
4	1.1645E-3
8	2.2969E-4
14	6.0652E-4
18	8.0405E-4
20	8.8195E-4
22	9.4953E-4
24	1.0075E-3

The deflection profile of the analytical arc model, along the neutral axis, was also compared with the FEA-predicted deformation. To make a direct comparison, the results of the analytical model were overlayed on top of the FEA results using the same scaling and aspect ratio (Figure 14). For a force of 40 kN and n = 20 segments, the analytical model shows very close agreement with the neutral axis of the FEA model. To examine the linear range of deformation, a force of 2000 N was also used for the analytical model in Figure 15. In this result, the deviation of the deflection profile from the FEA model is much more noticeable, although the approximation agrees well near the root. The segmented arc model might not be accurate enough to estimate the behavior of an SMA semicircular arc for smaller forces. This outcome could be influenced by the trends observed in the percent error of δ_y for small forces, shown in Table 4, since the analytical beam model is integral to the derivation of the segmented arc model.

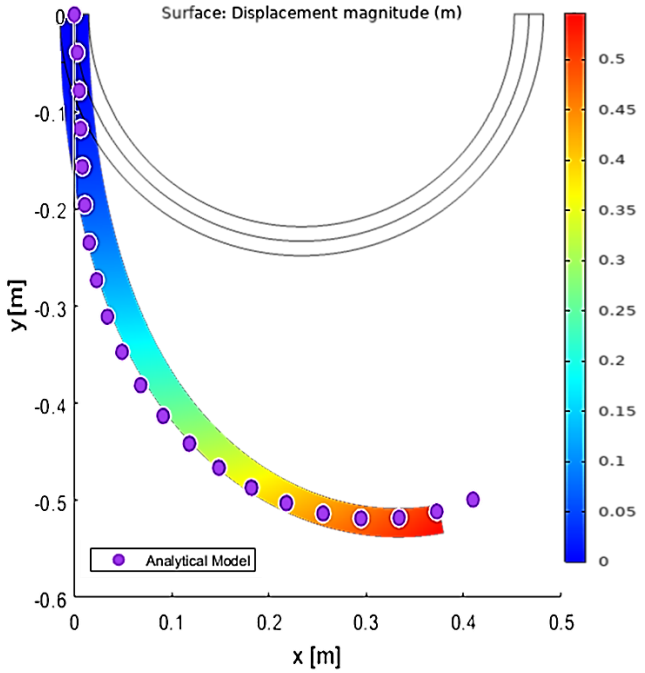

FIGURE 14: ANALYTICAL ARC MODEL DEFLECTION PROFILE ALONG THE NEUTRAL AXIS AND FEA MODEL DEFLECTION FOR N = 20 SEGMENTS AND A FORCE OF 40000 N

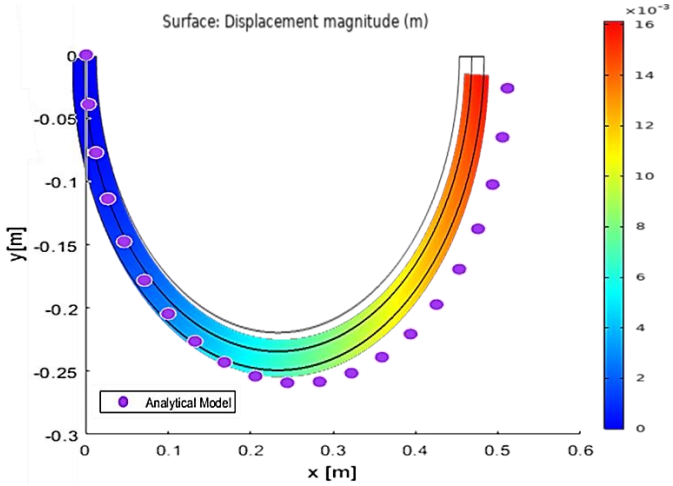

FIGURE 15: ANALYTICAL ARC MODEL DEFLECTION PROFILE ALONG THE NEUTRAL AXIS AND FEA MODEL DEFLECTION FOR N = 20 SEGMENTS AND A FORCE OF 2000 N

The location of the neutral axis changes depending on the extent of phase transformation due to the changing composition of solid phases within the SMA during phase transformation. By examining the stress-distribution of the FEA arc model, it is clear that the von Mises stress is not symmetric in tension and compression, as shown in Figure 16. The stress is lower on the compressive side than on the tension side.

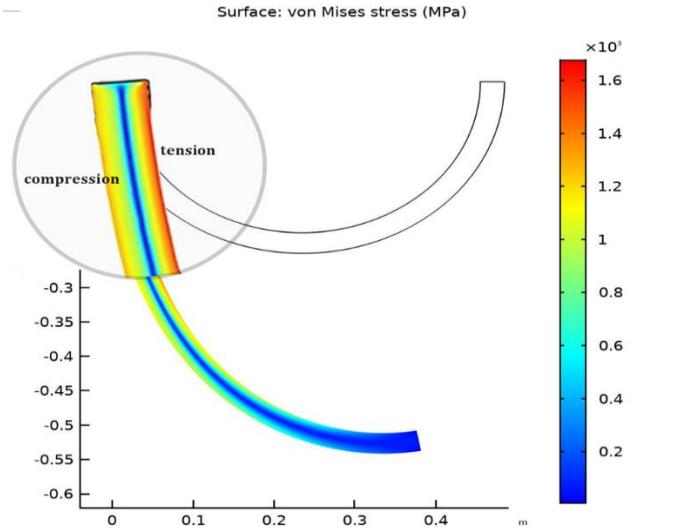

FIGURE 16: SEGMENTED ARC APPROXIMATION AND FEA MODEL DEFLECTION FOR N = 20 SEGMENTS AND A FORCE OF 2000 N

4. CONCLUSIONS

In this paper, an analytical model is developed for a compliant cantilever beam made of superelastic material experiencing large deformation. A segmentation approach is used to extend the beam model to a model of a semicircular compliant arc. In comparing the models to FEA simulations, the results indicate that the analytical model successfully captures the effect of the stress-induced phase transformation on large deflections for both the cantilever beam and semicircular arc cases. Differences in the analytical model compared to FEA could be attributed to the discrepancy in the x-coordinates used for the analytical and FEA models. The same number of points are sampled, but due to the analytical model being an iterative solver in x, the sampled points are not exactly at the same locations as those extracted from the FEA study. As a result, interpolation was done to resolve this issue. The effect that this result may have warrants further investigation in refining the current model, despite the relatively small mean-squared errors that were obtained.

An additional source of error can be related to the symmetry of the stress distribution in the model proposed by Eshghinejad et al. Prior research, such as analytical methods proposed by Viet et al. [16] for modeling SMA alloy beams, suggests that during loading, the neutral axis shifts with increasing tip load toward the compressive side of the deformed beam. The assumed symmetric stress distribution in the analytical model does not account for the tension-compression asymmetry in the bending of SMAs. This insight could explain the error that is seen in the deflection of the analytical cantilever beam model, specifically in Figure 9(a). In this plot, the neutral axis of the analytical model appears to deviate more from the FEA model when the applied tip load is large, or in the region of phase transformation. Similarly, the plots shown in Figures 7 and 8 show that the curvature profile of the FEA model deviates from the analytical solution as the tip load increases. This result could also be an influential factor in improving the accuracy of the analytical model. Future work should explore the effect of tension-compression asymmetry caused by the changing martensitic volume fraction within the SMA. Further research in this area can potentially improve the current analytical models by considering the shifting of the neutral axis during phase transformation of the SMA.

Ongoing work includes further investigation of the stress distribution in the three regions as predicted by the model and comparison to the stress-distribution given by FEA. Also, the neutral axis of the arc modeled in COMSOL should be extracted to find the mean square error between FEA and the analytical results. This would provide a clearer picture of how the neutral axis is changing in both models.

ACKNOWLEDGEMENTS

The first and third authors gratefully acknowledge the support of the Leighton Riess Professorship in Engineering at Penn State University.

REFERENCES

1. J. P. Calogero, M. I. Frecker, Z. Hasnain, and J. E. Hubbard, “Dual optimization of contact-aided compliant mechanisms for passive dynamic shape change,” AIAA J., vol. 56, no. 9, pp. 3745–3756, 2018.
2. B. V. S. N. Reddy, S. V. Naik, and A. Saxena, “Systematic synthesis of large displacement contact-aided monolithic compliant mechanisms,” J. Mech. Des. Trans. ASME, vol. 134, no. 1, pp. 1–12, 2012.
3. Y. Tummala, A. Wissa, M. Frecker, and J. E. Hubbard, “Design and optimization of a contact-aided compliant mechanism for passive bending,” J. Mech. Robot., vol. 6, no. 3, pp. 1–9, 2014.
4. V. Mehta, M. Frecker, and G. A. Lesieutre, “Two-step design of multicontact-aided cellular compliant mechanisms for stress relief,” J. Mech. Des. Trans. ASME, vol. 134, no. 12, pp. 1–12, 2012.
5. V. Mehta, M. Frecker, and G. A. Lesieutre, “Stress relief in contact-aided compliant cellular mechanisms,” J. Mech. Des. Trans. ASME, vol. 131, no. 9, pp. 0910091–09100911, 2009.
6. S. A. Cirone, G. R. Hayes, B. L. Babcox, M. Frecker, J. H. Adair, and G. A. Lesieutre, “Design of contact-aided compliant cellular mechanisms with curved walls,” Artic. J. Intell. Mater. Syst. Struct., vol. 23, no. 16, pp. 1773–1785.
7. J. E. Hyland, M. I. Frecker, and G. A. Lesieutre, “Optimization of honeycomb contact-aided compliant cellular mechanism for strain energy absorption,” in Proceedings of the ASME Design Engineering Technical Conf., 2012, vol. 4, no. PARTS A AND B, pp. 311–320.
8. J. Jovanova, A. Nastevska, and M. Frecker, “Tailoring energy absorption with functional grading of a

contact-aided compliant mechanism," Smart Mater. Struct., vol. 28, no. 8, 2019.
9. J. Jovanova, A. Nastevska, and M. Frecker, "Functionally graded cellular contact-aided compliant mechanism for energy absorption," in ASME 2018 Conference on Smart Materials, Adaptive Structures and Intelligent Systems, SMASIS 2018, vol. 2, 2018.
10. A. Nastevska, J. Jovanova, and M. Frecker, "Design of compliant joints for large scale structures," in ASME Conference on Smart Structures Adaptive Structures and Intelligent Systems, pp. 1–10, 2020.
11. F. Auricchio, R. L. Taylor, and J. Lubliner, "Shape-memory alloys: macromodelling and numerical simulations of the superelastic behavior," Computer Methods in Applied Mechanics and Engineering, vol. 146, pp. 281-312, 1997.
12. A. Eshghinejad and M. Elahinia, "Exact solution for bending of shape memory alloy beam," Mechanics of Advanced Materials and Structures, 22, pp. 829–838, 2015.
13. S. Ghuku and K. Saha, "A theoretical and experimental study on geometric nonlinearity of initially curved cantilever beams," Engineering Science and Technology, an International Journal, vol. 19, no. 1, pp. 135-146, 2016.
14. L. Chen, "An integral approach for large deflection cantilever beams," International Journal of Non-Linear Mechanics, vol. 45, pp. 301–305, 2010.
15. T. Hsu, "Determination of the moment-curvature relation for a beam of nonlinear material," The University of Arizona, 1966.
16. N. Viet, W. Zaki, and Z. Moumni, "A model for shape memory alloy beams accounting for tensile compressive asymmetry," Journal of Intelligent Material Systems and Structures, vol. 30, 2019.